

A clinically applicable laser-based image-guided system for laparoscopic liver procedures

Matteo Fusaglia¹ · Hanspeter Hess¹ · Marius Schwalbe¹ · Matthias Peterhans¹ · Pascale Tinguely² · Stefan Weber¹ · Huanxiang Lu¹

Received: 15 May 2015 / Accepted: 24 September 2015
© CARS 2015

Abstract

Purpose Laser range scanners (LRS) allow performing a surface scan without physical contact with the organ, yielding higher registration accuracy for image-guided surgery (IGS) systems. However, the use of LRS-based registration in laparoscopic liver surgery is still limited because current solutions are composed of expensive and bulky equipment which can hardly be integrated in a surgical scenario.

Methods In this work, we present a novel LRS-based IGS system for laparoscopic liver procedures. A triangulation process is formulated to compute the 3D coordinates of laser points by using the existing IGS system tracking devices. This allows the use of a compact and cost-effective LRS and therefore facilitates the integration into the laparoscopic setup. The 3D laser points are then reconstructed into a surface to register to the preoperative liver model using a multi-level registration process.

Results Experimental results show that the proposed system provides submillimeter scanning precision and accuracy comparable to those reported in the literature. Further quantitative analysis shows that the proposed system is able to achieve a patient-to-image registration accuracy, described as target registration error, of 3.2 ± 0.57 mm.

Conclusions We believe that the presented approach will lead to a faster integration of LRS-based registration techniques in the surgical environment. Further studies will focus

on optimizing scanning time and on the respiratory motion compensation.

Keywords Image-guided surgery · Laparoscopic liver surgery · Laser range scanner · Surface registration

Introduction

Clinical context

Laparoscopic liver procedures provide significant benefits including reduced postoperative discomfort, hospital stay and recovery time as they eliminate the need for large abdominal wall incisions. During laparoscopy, a two-dimensional (2D) video camera is introduced into the patient's abdomen, providing visual information regarding the surgical situs and instrument positions. Nevertheless, main drawbacks of this procedure are the loss of depth perception and tactile feedback. These aspects weaken the spatial understanding and increase the risk of undesired contact between instruments and anatomical structures. For these reasons, performing laparoscopic liver procedures requires significant hand-eye coordination and extensive training experience.

The aforementioned disadvantages of laparoscopic liver procedures can be addressed by the use of image-guided surgery (IGS) [1]. IGS systems map tracked surgical instruments, preoperatively computed 3D anatomical models from computer tomography (CT) or magnetic resonance imaging (MRI) and intraoperative patient data into an identical coordinate system through a registration method [2, 3]. Obtaining an accurate patient-to-image registration represents a key aspect in the successful use of IGS technologies in laparoscopic liver procedures.

✉ Matteo Fusaglia
matteo.fusaglia@artorg.unibe.ch

¹ Artorg Center for Biomedical Engineering Research, IGT, University of Bern, Bern, Switzerland

² Department of Visceral Surgery, University Hospital of Bern, Bern, Switzerland

State of the art

Various registration methods have been proposed in the literature, which can be classified into two categories in terms of the acquisition method of the intraoperative patient data.

The first category relies on a sweeping process of an instrument or ultrasound (US) probe on the liver to generate a surface or 3D anatomical model. Herline et al. presented a surface-based registration method for soft tissue surgery where a set of 3D points are intraoperatively acquired and matched to the preoperative 3D model [4]. The intraoperative acquisition is performed by manually sweeping or touching the organ's surface with a tracked instrument. Alternatively, Lange et al. proposed to manually sweep a tracked ultrasound probe over the liver surface to acquire an intraoperative 3D model of vessels. This vascular model is then registered to the preoperative 3D model by matching the centerline of the vessel using an iterative closest point (ICP) approach [5]. While these registration methods require simple settings and promising results were reported, one drawback is that they apply pressure to the organ due to required physical contact of the instruments/probes with the liver. This pressure deforms the intraoperative liver shape, thus hindering the registration accuracy [6]. Non-rigid registration could potentially compensate for the deformation [5], but it results in significantly more computational time which is not available in the operating room.

The second category acquires the intraoperative model by avoiding physical contact through a tracked laser range scanner (LRS). An LRS exploits the principle of triangulation to determine the 3D position of a laser reflection, which is detected by a digital camera. Through a tracked LRS, it is possible to acquire an intraoperative set of 3D points of the liver in the native IGS coordinate system and register it to the preoperative 3D model. LRS-based registration methods avoid physical contact during the organ scanning, thus eliminating deformation in the whole registration process and potentially leading to higher accuracy.

Commercial LRSs have been extensively utilized for registration in image-guided neurosurgery (IGNS) and image-guided liver surgery (IGLS). In [7], a commercial LRS was utilized for registration and characterization of intra-surgical brain deformation in the context of IGNS and evaluated by automatically scanning a brain phantom. In [8], a commercially available laser scanner (z-touch, BrainLAB, Feldkirchen, Germany), which was optically tracked, was utilized in a 36-patient study for patient-to-image registration in the context of IGNS. By manually sweeping the laser scanner over a region of interest, the authors reported a target localization error of 2.7 ± 1.6 mm for the surgical field. Additionally, they reported that LRS-based registra-

tion is a valuable alternative to marker-based registration. A comparison between LRS and point-based registration (PBR) indicates that the LRS-based registration provides a lower registration error (0.8 ± 0.3 mm) than PBR (1.9 ± 1.0 mm) [9]. In another study, aimed at targeting structures within keyhole neurosurgery, an intraoperative manual surface scan of the patient's facial features, acquired with an LRS, was registered to a preoperative image [10]. The system's registration accuracy was evaluated on a phantom and showed a target registration error of 1.7 ± 0.7 mm. Cash et al. reported the integration of an LRS into an IGLS system for registration and evaluated its accuracy by automatically scanning a liver phantom. After an initial PBR alignment, a mean surface residual error of 0.75 mm and mean TREs of 2.0 and 4.1 mm for two different sets of targets were observed [11]. Similar findings were reported in [12].

Despite commercial LRS having led to promising results in conventional IGS, their use in laparoscopic procedures is challenging because a line of sight from LRS to the liver is missing. This is because during laparoscopy, the liver is not exposed as in the case of open surgery, and therefore cannot be scanned by commercial LRS. Furthermore, in laparoscopy, the LRS systems would require sterilizability, which is usually missing in commercial LRS, due to the direct contact with the patient. Several initial attempts have been presented in the past decade. Hayashibe et al. introduced an LRS system for laparoscopic image guidance, which is composed of a high-speed camera, a 2D galvano scanner and a laser for 3D shape recovery and registration [13]. The system's accuracy was evaluated by automatically scanning tracked objects (e.g., a plane and a sphere) and computing the average distance between the tracked objects and the acquired set of 3D points. For each scan, a set of 8000 3D points was acquired. An average error of 0.16 mm and maximum errors of 1.0 and 1.5 mm were estimated, respectively, for the plane and the sphere. A liver phantom was also scanned in a previous work, but only a qualitative evaluation regarding the accuracy of the registration was presented [14]. The aforementioned system was also extended for detecting liver deformation and was applied during an in vivo animal experiment where improved depth perception was achieved. A similar LRS system, presented by Friets et al., demonstrated a scanning accuracy of 0.38 ± 0.27 mm for objects of known geometry placed at different distances to the LRS [15]. A system based on conoscopic holography was presented in [6] where, by manually scanning a phantom, a mean TRE accuracy of 2.94 mm was found. Additional results of this system [22] showed a surface registration error of 1.73 ± 0.77 and 1.5 ± 0.5 mm, respectively, on ex vivo porcine liver and human kidney specimen. A summary of the aforementioned surface-based registration techniques together with their target applications is shown in Table 1.

Table 1 Summary of surface-based registration methods relevant for this work

Acquisition method	Work	Sweep modality	Application
Contact	Herline et al. [4]	Manual	Open liver surgery
	Lange et al. [5]	Manual	Open liver surgery
Contactless	Audette et al. [7]	Automatic	Neurosurgery
	Schlaier et al. [8]	Manual	Neurosurgery
	Mcdonald et al. [9]	Manual	Orthopedic surgery
	Joskowicz et al. [10]	Manual	Neurosurgery
	Cash et al. [11]	Automatic	Open liver surgery
	Dumpuri et al. [12]	Automatic	Open liver surgery
	Hayashibe et al. [13]	Automatic	Laparoscopic general surgery
	Friets et al. [15]	Manual	Laparoscopic kidney surgery
Lathrop et al. [6]	Manual	Laparoscopic liver surgery	

Problem description

To date, there is a lack of clinical experimental results pertaining to the application of LRS-based image guidance for laparoscopic procedures. This may derive from the fact that the current custom-made LRSs are composed of bulky equipment such as high-speed or time-of-flight cameras and actuators. These devices are difficult to integrate into a laparoscopic scenario due to the smaller size of the laparoscopic incision (i.e., 5–10 mm). For these reasons, the LRS for laparoscopic procedures has to satisfy specific size constraints (i.e., a diameter inferior than 10 mm). Furthermore, LRSs for laparoscopic procedures have to be easily handheld to facilitate the insertion in the abdominal cavity.

While attempts have been made to reduce the size of LRS, this is not a trivial task since LRS usually requires large displacement between the laser emitter and the receiver to keep high precision of the scanning [16, 17]. In addition, the high cost of this equipment relegates the use of LRS-based systems to a small niche.

Contributions and overview of the manuscript

In this work, we present a new compact and cost-effective LRS for image-guided laparoscopic procedures and integrate into a commercially available IGS system (CAScination AG, Switzerland). Through a triangulation process, the 3D coordinate of the laser pointer is obtained by using only the laser emitter. This allows to discard the laser receiver, hence significantly reducing the size of the LRS. The key contributions of this work are:

- A compact LRS specifically designed for laparoscopic procedures composed of a commercial laser pointer and a sterilizable encasement.
- A novel triangulation formulation that allows the integration of the LRS into a commercially available IGS.

- Automatic patient-to-image registration without the need of additional imaging devices such as high-speed or time-of-flight cameras.
- Evaluation of the efficacy of the proposed system by analyzing the LRS scanning accuracy and the registration accuracy.

The paper is organized as follows. In “Materials and methods” section, we present the principle of the system including the triangulation formulation for mapping the set of 3D points into the IGS coordinate system, the instrument design and calibration, and the patient-to-image registration algorithm. The evaluation on liver phantoms is elaborated in “Results” section, followed by the results described in “Discussion” section. In “Conclusion” section, we conclude our work by discussing the obtained findings as well as the future work to address the potential drawbacks of the current system.

Materials and methods

System overview

A commercial IGS system for open liver procedures (CAScination AG, Bern, Switzerland) was extended with laparoscopic instrument tracking capabilities and a software module for image visualization and processing. Instrument tracking is accomplished by attaching retro-reflective spheres onto the laparoscope and laser, which can be tracked by a passive optical tracking system (NDI Vicra, Northern Digital, Canada). The IGS system provides the tracking information as transformation matrices in a common coordinate system (i.e., world coordinate system). By tracking the instruments, it is possible to determine their pose and compute the intersection between the laparoscope’s optical axis and the laser beam. This procedure, also called triangulation, defines the 3D coordinate of a laser point detected in the laparoscope

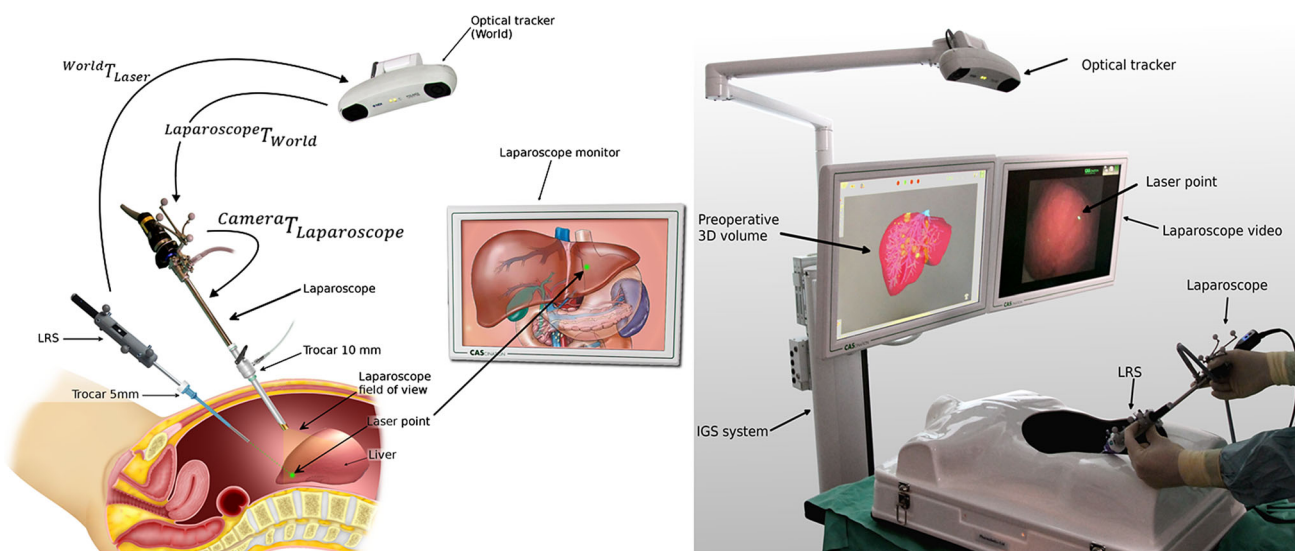


Fig. 1 Left functional system's model and employment design. Right IGS system setup

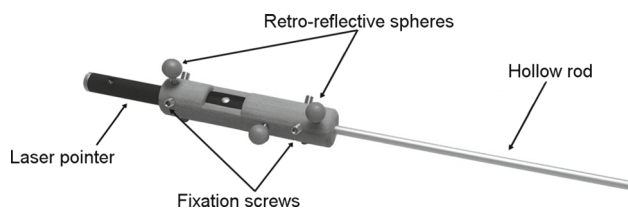


Fig. 2 Laser tool composed of a laser pointer and a trackable encasement. The hollow rod allows the insertion of the tool in the patient's abdomen

image. Figure 1 depicts the functional IGS model and its use with the LRS.

The LRS consists of a commercially available green-laser pointer (output of 5 mW at 532 nm) and a trackable encasement composed of a rapid prototyped shaft, three retro-reflective spheres and a hollow rod. The hollow rod allows the instrument to be inserted into the patient's abdomen and the laser to scan the organ. Six screws are placed along the radial axis of the encasement ensuring a unique and fixed positioning of the laser (Fig. 2). This aspect facilitates clinical integration: The laser pointer can be packed within a sterile bag, while the encasement is sterilizable. Intraoperatively, the laser would be inserted into the encasement in a unique configuration eliminating the need for intraoperative calibration. Thereafter, the LRS would be inserted into the patient's abdomen through a standard trocar allowing a direct line of sight to the liver which is required for the intraoperative scan (Fig. 1).

Triangulation of LRS

The triangulation of LRS allows the definition of the 3D coordinate of a laser point detected in the laparoscope image.

Prior to this process, the laparoscope and the laser pointer are calibrated. A standard 0° laparoscope (Olympus Evis Exera II, Japan) is optically calibrated by attaching an optical marker using the methodology described in [18]. The laparoscope calibration allows estimating the intrinsic parameters (i.e., focal length, principal point), the extrinsic parameters (i.e., transformation which maps the optical center to the optical marker) and the distortion coefficients. Through the distortion coefficient, it is possible to compensate for radial and tangential distortion, introduced by the laparoscope lenses, yielding to a rectified image. This aspect is particularly relevant in laparoscope cameras where the wide angle creates high convex images which, if not rectified, would lead to convex scans. By using a general optical calibration methodology, the system is independent from the laparoscope camera manufacture specifications, increasing its flexibility to be employed with different laparoscopic system. The laser pointer is calibrated by aligning the laser beam with the rod and by digitizing the rod's geometry and the spheres through a position measurement system.

Mathematically, the 2D laser point's coordinate in the laparoscope image is a projection of 3D coordinate in the world system defined by the optical tracking.

$$\begin{bmatrix} su \\ sv \\ s \end{bmatrix}_{\text{Image}} = A \cdot \begin{bmatrix} R & t \end{bmatrix} \begin{bmatrix} X \\ Y \\ Z \\ 1 \end{bmatrix}_{\text{World}}, \tag{1}$$

where $(X Y Z 1)_{\text{World}}$ denotes the laser point in homogeneous world coordinate, s is a nonzero scaling factor, $(su sv s)_{\text{Image}}$ denotes the corresponding point in homogeneous image coordinates. A encodes the intrinsic parameters

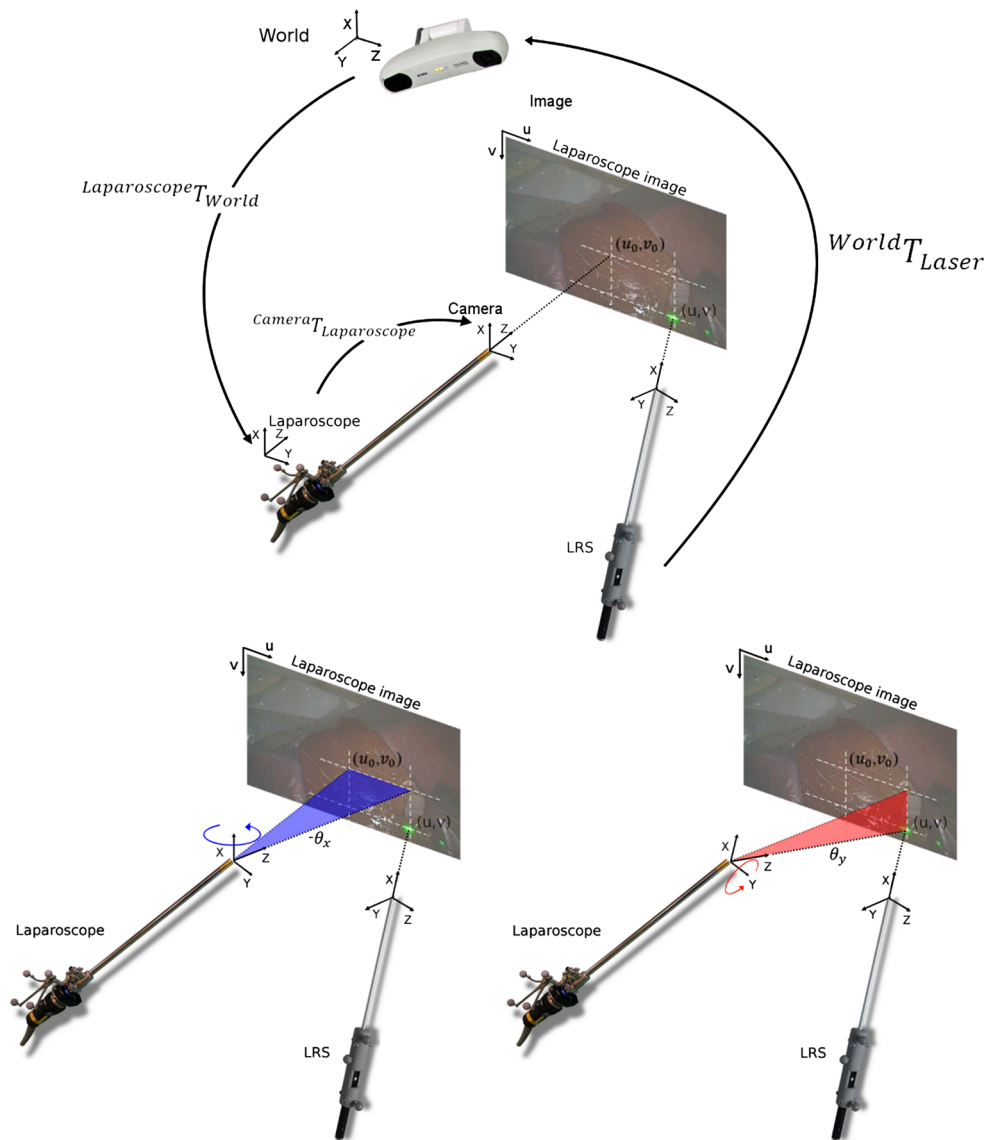


Fig. 3 Triangulation through a rotation process of the laparoscope coordinate system. *Top* initial configuration. *Bottom left*: rotation around the x axis. *Bottom right*: rotation around the y axis

obtained from the laparoscope calibration, and $[R \ t]$ is a transformation from the world coordinate system to the camera coordinate system.

Since the laparoscope is tracked, given the transformation from the camera to the laparoscope marker, $[R \ t]$ can be defined as:

$$[R \ t] = {}^{Camera}T_{Laparoscope} \cdot {}^{Laparoscope}T_{World},$$

where ${}^{Laparoscope}T_{World}$ is the transformation from the world to the laparoscope coordinate system provided by the tracking system, and ${}^{Camera}T_{Laparoscope}$ is the transformation from the marker to the camera, provided by the previous laparoscope calibration (Fig. 3 top). Equation (1) can be rewritten as:

$$\begin{bmatrix} su \\ sv \\ s \end{bmatrix}_{Image} = {}^{Image}A_{Camera} \cdot {}^{Camera}T_{Laparoscope} \cdot {}^{Laparoscope}T_{World} \cdot \begin{bmatrix} X \\ Y \\ Z \\ 1 \end{bmatrix}_{World}, \quad (2)$$

If the laser point's coordinate in the laparoscope image is coincident with the image's center (i.e., principal point), the 3D coordinate of the laser point $(X \ Y \ Z \ 1)_{World}$ is determined as the intersection between the laser's beam and the laparoscope's optical axis. The laser's beam and the laparoscope's optical axis are, respectively, coincident with the x

and z axis in their own coordinates system. Given the transformations that map the laser's beam and the laparoscope's optical axis in the image coordinate system, Eq. (2) can be described as:

$$\begin{bmatrix} su \\ sv \\ s \end{bmatrix}_{Image} = {}_{Image}A_{Camera} \cdot \begin{bmatrix} 0 \\ 0 \\ Z \\ 1 \end{bmatrix}_{Camera} = {}_{Image}A_{Camera} \cdot {}_{Camera}T_{Laparoscope} \cdot {}_{Laparoscope}T_{World} \cdot {}_{World}T_{Laser} \cdot \begin{bmatrix} X \\ 0 \\ 0 \\ 1 \end{bmatrix}_{Laser}, \tag{3}$$

where ${}_{World}T_{Laser}$ is the transformation from the laser to the world coordinate system provided by the tracking system; $(0 \ 0 \ Z \ 1)_{Camera}$ and $(X \ 0 \ 0 \ 1)_{Laser}$ are the principle point and laser point in the camera coordinate and laser coordinate, respectively, which can be obtained by solving the above linear system. The 3D coordinate of the laser point $(X \ Y \ Z \ 1)_{World}$ can then be computed by mapping $(X \ 0 \ 0 \ 1)_{Laser}$ into the world coordinate.

Conversely, if the laser point's coordinate and the principal point are initially different, a rotational transformation is performed in the camera coordinate system (Fig. 3 bottom). This rotation allows to intersect the z axis of the laser point in the image and is expressed as a product of two basic rotations R_x and R_y using the angles:

$$\theta_x = \tan^{-1} \frac{u - u_0}{f_u}$$

$$\theta_y = -\tan^{-1} \frac{(v - v_0) \cdot \frac{f_u}{f_v}}{\sqrt{f_u^2 + (u - u_0)^2}},$$

where (u_0, v_0) describe the principal point and (f_u, f_v) the focal lengths, also obtained through the optical calibration of the laparoscope. Equation (3) is then extended to:

$$\begin{bmatrix} su \\ sv \\ s \end{bmatrix}_{Image} = {}_{Image}A_{Camera} \cdot \begin{bmatrix} R_x R_y & 0 \\ 0 & 0 \\ 0 & 0 \\ 0 & 0 \ 0 \ 1 \end{bmatrix} \cdot \begin{bmatrix} 0 \\ 0 \\ Z \\ 1 \end{bmatrix}_{Camera} = {}_{Image}A_{Camera} \cdot {}_{Camera}T_{Laparoscope} \cdot {}_{Laparoscope}T_{World} \cdot {}_{World}T_{Laser} \cdot \begin{bmatrix} X \\ 0 \\ 0 \\ 1 \end{bmatrix}_{Laser}, \tag{4}$$

where $R_x R_y$ is the transformation which encode the rotations θ_x and θ_y .

In reality, the laser's beam and the laparoscope's optical axis do not necessarily intersect due to tracking and calibration errors. To account for this skewness, the midpoint which lies on the intersecting line perpendicular to the laser's beam and the optical axis is determined. This line

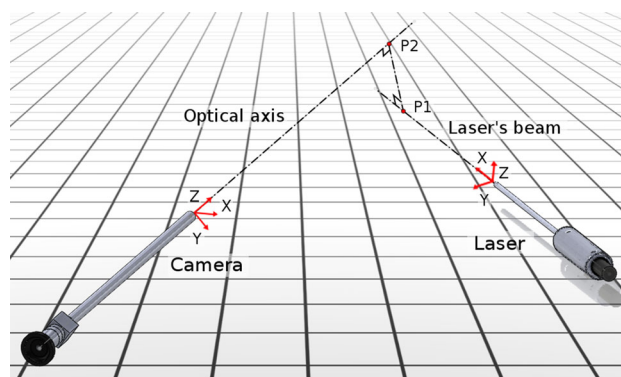


Fig. 4 To account for the skewness of the laser's beam and the laparoscope's optical axis, P_1 and P_2 define a line that is perpendicular to the beam and the optical axis. The midpoint of this line is defined as the 3D coordinate of the laser point

determines two points, P_1 and P_2 , which lie, respectively, on the laser's beam and the laparoscope's optical axis. P_1 is defined as $(X_1 \ 0 \ 0)_{Laser}$ in the laser coordinate system and as $(X_1 \ Y_1 \ Z_1)_{Camera}$ in the camera coordinate system. Conversely, P_2 is defined as $(0 \ 0 \ Z_2)_{Camera}$ in the camera coordinate system and as $(X_2 \ Y_2 \ Z_2)_{Laser}$ in the laser coordinate system. Because the shortest line segment between P_1 and P_2 is perpendicular to the beam and the optical axis, the X component of P_1 in the laser coordinate system (i.e., $X_1 \text{ Laser}$) is equal to the X component of P_2 in the laser coordinate system (i.e., $X_2 \text{ Laser}$). At the same time, the Z component of P_2 in the camera coordinate system (i.e., $Z_2 \text{ Camera}$) is equal to the Z component of P_1 in the camera coordinates system (i.e., $Z_1 \text{ Camera}$) (Fig. 4). Since $X_1 \text{ Laser} = X_2 \text{ Laser}$ and $Z_1 \text{ Camera} = Z_2 \text{ Camera}$ a linear system with six unknowns can be derived from Eq. 4. The following set of linear equations can be defined to solve P_1 and P_2 and the midpoint, defined as $\frac{P_1 + P_2}{2}$.

$$\begin{aligned} & {}_{Image}A_{Camera} \cdot \begin{bmatrix} R_x R_y & 0 \\ 0 & 0 \\ 0 & 0 \\ 0 & 0 \ 0 \ 1 \end{bmatrix} \cdot \begin{bmatrix} 0 \\ 0 \\ Z_1 \\ 1 \end{bmatrix}_{Camera} \\ & = {}_{Image}A_{Camera} \cdot {}_{Camera}T_{Laparoscope} \cdot {}_{Laparoscope}T_{World} \cdot {}_{World}T_{Laser} \cdot \begin{bmatrix} X_2 \\ Y_2 \\ Z_2 \\ 1 \end{bmatrix}_{Laser}, \end{aligned} \tag{5}$$

$$\begin{aligned} & {}_{Image}A_{Camera} \cdot \begin{bmatrix} R_x R_y & 0 \\ 0 & 0 \\ 0 & 0 \\ 0 & 0 \ 0 \ 1 \end{bmatrix} \cdot \begin{bmatrix} X_1 \\ Y_1 \\ Z_1 \\ 1 \end{bmatrix}_{Camera} \\ & = {}_{Image}A_{Camera} \cdot {}_{Camera}T_{Laparoscope} \cdot {}_{Laparoscope}T_{World} \cdot {}_{World}T_{Laser} \cdot \begin{bmatrix} X_2 \\ 0 \\ 0 \\ 1 \end{bmatrix}_{Laser}, \end{aligned} \tag{6}$$

Surface model acquisition

To reconstruct the intraoperative surface model, a sweep of the laser scanner is performed on the liver to acquire a set of 2D laser points on the laparoscopic image. These 2D points are then transformed into 3D coordinates using the triangulation to build a surface model of the liver.

An automatic 2D point detection algorithm is developed. Due to the good visibility of the laser point in the laparoscopic video, this detection is simply achieved using an RGB threshold algorithm. The laser point coordinate is computed as the centroid of the thresholded region. Since multiple regions may appear due to strong and specular reflections, the algorithm is extended with local criteria labeling a region as laser spot if:

1. The region's area is greater than 10 pixels;
2. All pixels representing the laser region are in a window of size 50×50 pixels.

If a region does not meet these criteria, it is considered as reflection and therefore discarded from the computation of the centroid. The design of a simple automatic 2D point detection algorithm guarantees a fast and constant data acquisition rate (i.e., approximately 20Hz).

Patient-to-image registration

The patient-to-image registration maps automatically the acquired laser surface model to the preoperative 3D liver model. The registration process is composed of two phases: First, it starts with a coarse alignment of three principal directions to avoid local minima and accelerate the computation. Then, a fine registration is performed to refine the accuracy.

The coarse alignment between the 3D point set and the preoperative volume is composed of three steps: Initially, the

best fitting plane of the 3D point set is determined. Then, the preoperative volume is shifted behind the best fitting plane, with the tracker's y-z plane and the preoperative volume sagittal plane parallel to each other. Finally, the preoperative volume is sequentially translated and rotated stepwise in three principal directions:

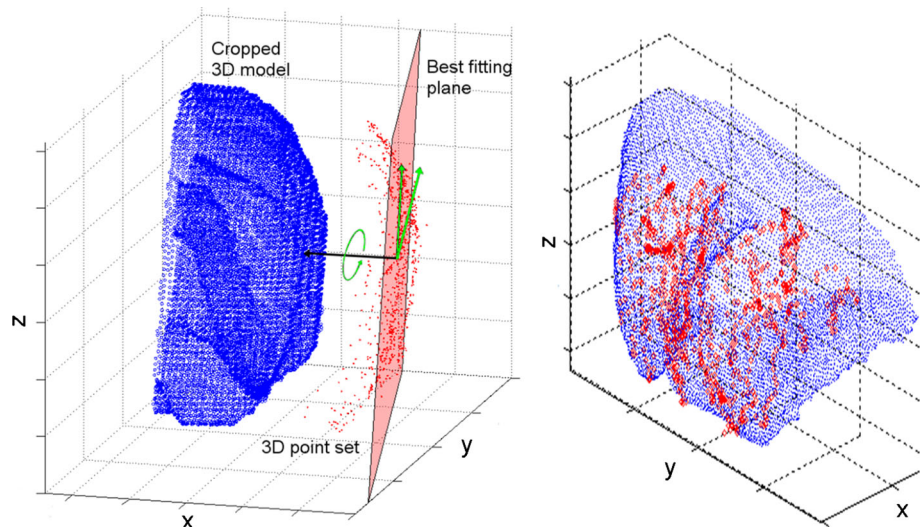
1. Perpendicular to the best fitting plane;
2. Parallel to the best fitting plane and perpendicular to the initial translation;
3. Around the axis normal to the best fitting plane.

To account for local minima, we divide each principal direction into multiple subspaces, where iterative closest point (ICP) matching is computed (Fig. 5). Then, an exhaustive search of the lowest RMS matching error among the subspaces is performed, and the resulting transformation is chosen as the initialization for the subsequent principal direction. Typically, 20 subspaces of size 10mm are chosen for the translational directions and 10 subspaces of size 10° are chosen for the rotational direction.

The incentive of choosing these three directions is under the assumption that the relative displacement between the organ, the acquired laser 3D point set and the tracker is approximately constant. In a clinical scenario, this is also plausible because the IGS system is positioned in approximately the same location for all procedures. The position of the IGS system is at the top of the operating table with the tracker over the patient's head. An optimal alignment is therefore determined through the coarse alignment which compensate for mispositioning the IGS system during the operation.

Finally, a fine ICP-based registration is computed from the transformation derived in the coarse alignment phase. For each phase, the ICP is computed by selecting all the acquired 3D point set and a cropped point set of the pre-

Fig. 5 Steps involved in the coarse registration. *Left* the best fitting plane from the 3D point set (*red point*) and the cropped 3D volume (*blue points*) is translated and rotated (*green arrows*). *Right* registration of the point set with the 3D model



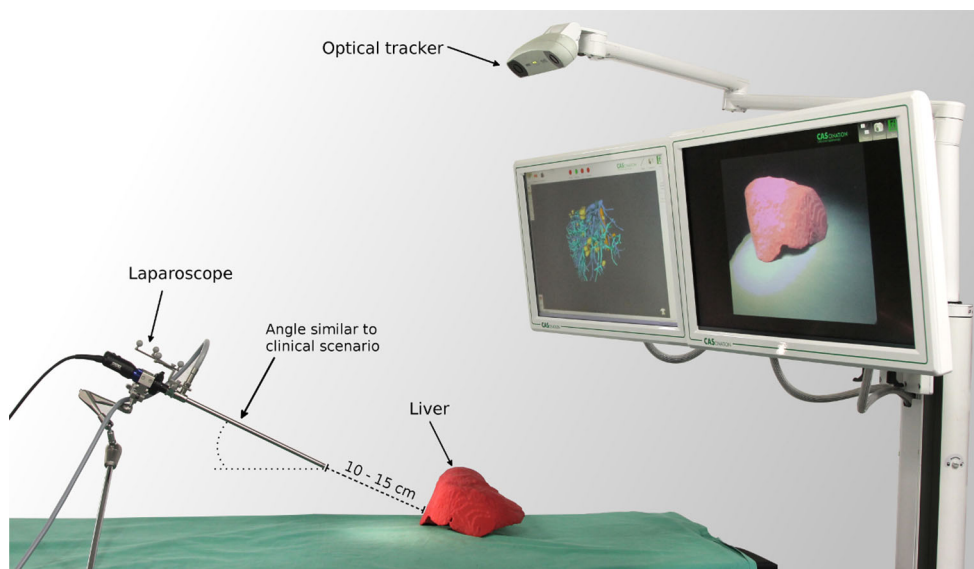


Fig. 6 Experiments setup

operative volume, representing the visible side of the liver during laparoscopy. The matching between the two point sets, defined as a partial correspondence problem, is computed through a nearest neighbor search, and constant weights are defined for each corresponding point pairs. Point-to-point minimization [19] is used as error metric and solved according to [20].

Experiments

Three experiments were designed to evaluate the LRS performances. First, the accuracy in determining the laser coordinate in the laparoscopic image was measured. Subsequently, the LRS accuracy and precision in scanning objects of known dimensions were evaluated. Finally, the accuracy in registering preoperative models to their real counterparts was assessed.

During the experiments, the IGS system was positioned at the top of the operating table with the tracker over the patient's head. Prior to the scanning procedure, the endoscope was calibrated and fixed in a stable configuration at a distance of approximately 10–15 cm from the objects (Fig. 6). This setup is under real scenario configurations to simulate the procedures in the operating room. Finally, the laser was manually swept over the objects surface to acquire the intraoperative scan. The scanning time was approximately 1 minute for 1000 3D points.

Accuracy of 2D point detection

To verify the algorithm's accuracy in detecting the laser coordinate, a ground-truth dataset was designed. This dataset was obtained by manually and carefully detecting the laser coordinate in a 295-image dataset, where the laser was directed

onto different materials (e.g., liver phantom and bovine tissue) under variable light conditions (e.g., ambient light and endoscopic light). The mean Euclidean distance between the automatically and manually detected coordinates was chosen as the accuracy metric.

Surface scanning precision and accuracy

To determine the LRS scanning accuracy and precision, the experiments presented by Hayshibe et al. [13], Lathrop et al. [6] and Friets et al. [15] in scanning objects of known dimensions were reproduced. A tracked plane (150 × 90 mm) and a sphere ($\varnothing = 50.85$ mm) were scanned. Two datasets of 4036 and 4663 3D points were acquired for the plane and the sphere, respectively, and their geometric surface fit was computed.

To determine the scanning precision of 3D point acquisition, the variability of the 3D point cloud from the surface fit was computed. Precision of the surface scan was defined as:

$$\text{Precision} = \frac{\sqrt{\sum_{i=1}^n (q_i - p_i)^2}}{n}, \quad (7)$$

where n is the number of scanned points, $q_i : i = 1, \dots, n$ is the set of scanned points, and p_i is the closest point to q_i which lies on the fitted surface.

To determine the scanning accuracy in reconstructing the actual object surfaces, the mean Euclidean distances from each acquired 3D point to the tracked plane and the actual sphere surface (using the actual sphere radius in place of the fit radius) were computed. Accuracy of the surface scan was defined as projection error:

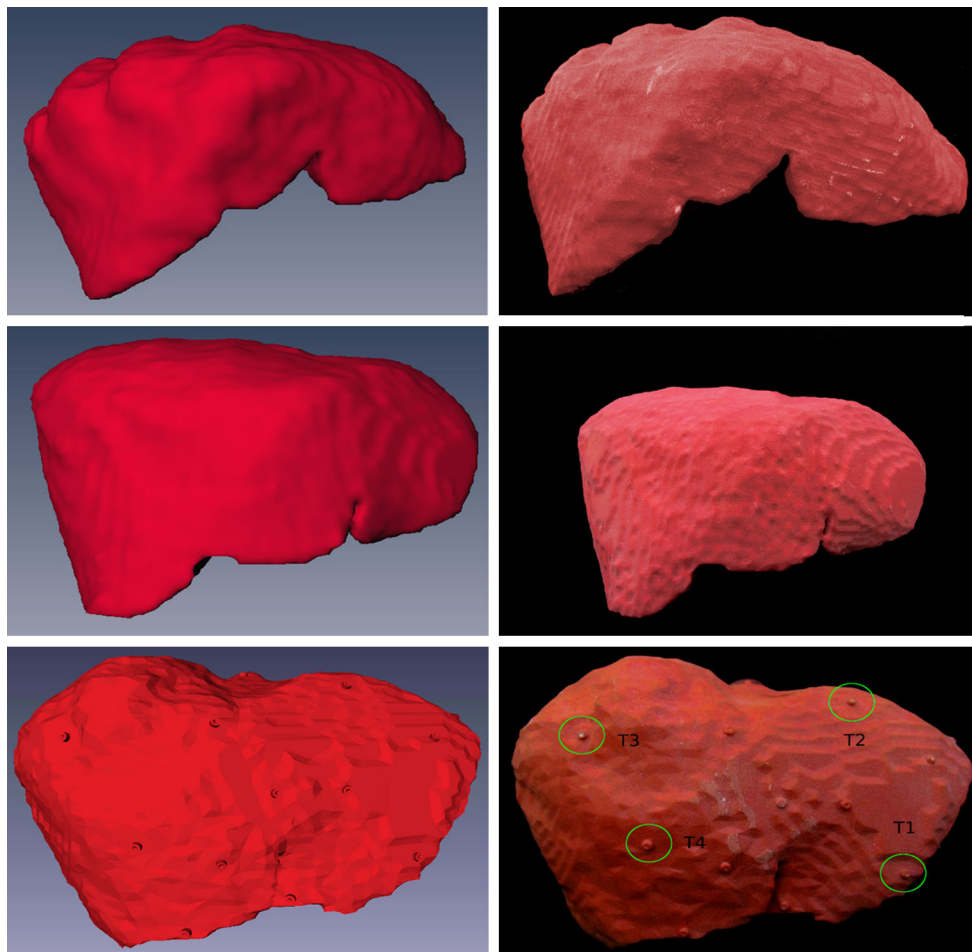


Fig. 7 Preoperative 3D volumes (*left*) and 3D printed models (*right*) used during the experiments. T1, T2, T3, T4 in *bottom right* represent the fiducials used for computing the target registration error

$$\text{Accuracy} = \frac{\sqrt{\sum_{i=1}^n (q_i - r_i)^2}}{n}, \quad (8)$$

where n is the number of scanned points, $q_i : i = 1, \dots, n$ is the set of scanned points, and p_i is the closest point to r_i which lies on the real surface.

Patient-to-image registration accuracy

To evaluate the accuracy pertaining to the registration of the preoperative models to the real objects, an experiment was performed on a set of patient-specific phantoms built by rapid prototyping. Within the experiment, three scans of 2000 3D points were performed on three liver phantoms (Fig. 7). Each acquired point set was partitioned into subsets of 600 3D points which were automatically registered with their respective preoperative models. The liver surface models were reconstructed from clinical image datasets, and the physical models were realized using a rapid prototyping machine (Spectrum 510, Z-Corp, Rock Hill, USA).

In addition to the RMS error, the mean surface residual error, as defined in [11], was computed. In addition, four fiducials (\varnothing 4mm) on the surface of one liver model were digitized with an optically tracked pointer, and the target registration error (i.e., TRE) at each fiducial for each registration was computed. Figure 7 bottom right depicts the fiducials used as targets. To minimize the influence of the tracking error, each landmark position was determined as the average of 10 individual measurements.

A sensitivity analysis aimed at evaluating the effects of the number of acquired 3D points on the registration accuracy, was also conducted. This aspect is particularly important given the scanning time (approximately 30 seconds for each dataset) which might be a drawback in the clinical scenario, due to the liver respiratory movement. Based on an initial 2000 3D point set, different registrations were performed by varying the number of 3D points. The accuracy of the registrations was assessed by recording the TRE for the aforementioned fiducials.

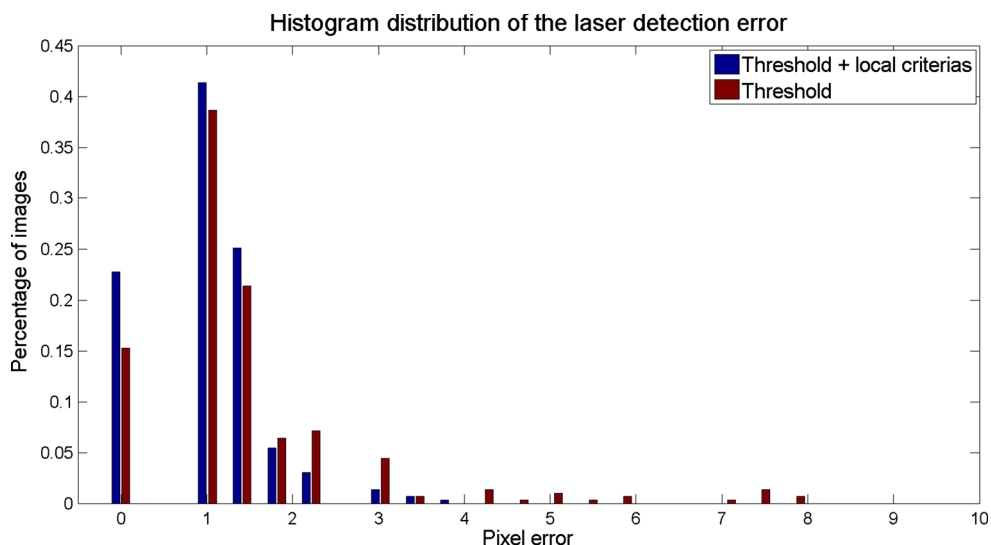


Fig. 8 Normalized error histogram distribution of the threshold algorithm (*red*) and the local criteria algorithm (*blue*)

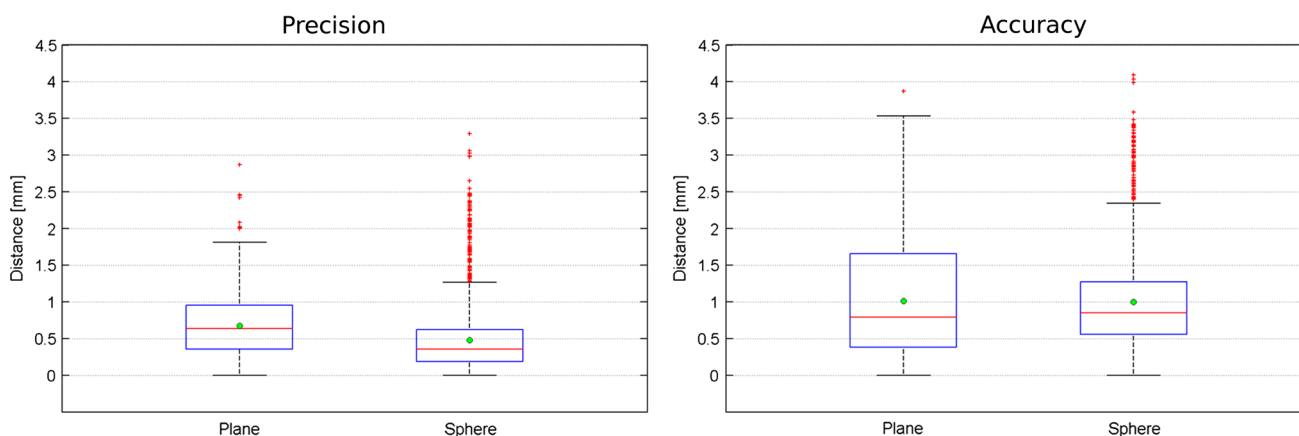


Fig. 9 LRS precision (*left*) and accuracy (*right*) in scanning objects of known dimension. The *green circles* represent the average distance

Results

Accuracy of 2D point detection

The local criteria used in the 2D point detection are expected to improve the detection of the correct laser coordinates in the presence of reflections and variable lighting. Subsequently, a higher accuracy and a lower standard deviation error compared with a threshold-based algorithm can be expected. The threshold-based algorithm achieved an accuracy of 1.4 ± 1.3 pixels, whereas this accuracy dropped to 1.0 ± 0.7 pixels when the local criteria were applied. The error histogram distribution in detecting the laser coordinate for both algorithms is depicted in Fig. 8. The detection error between the two algorithms was significantly different ($\rho \leq 0.05$, using Fisher's f-test) for all datasets (i.e., phantom, bovine, ambient light, endoscopic light).

Surface scanning precision and accuracy

The precision and accuracy in scanning objects of known dimensions are summarized in Fig. 9. Average submillimeter precision is achieved in both objects (represented as green circles in Fig. 9). Figure 10 provides a visual representation of the 3D points acquired through the scanning process and the respective best fitting geometries. The accuracy of the proposed method in reconstructing a sphere is comparable to the accuracy reported in the literature [13]. The reconstruction error defined as the ratio between the fitted radius (24.54 mm) and the actual radius (25.42 mm) is below 5%.

Patient-to-image registration accuracy

For each liver phantom, 20 registrations were performed, yielding a residual error of 1.27 ± 0.75 mm and an aver-

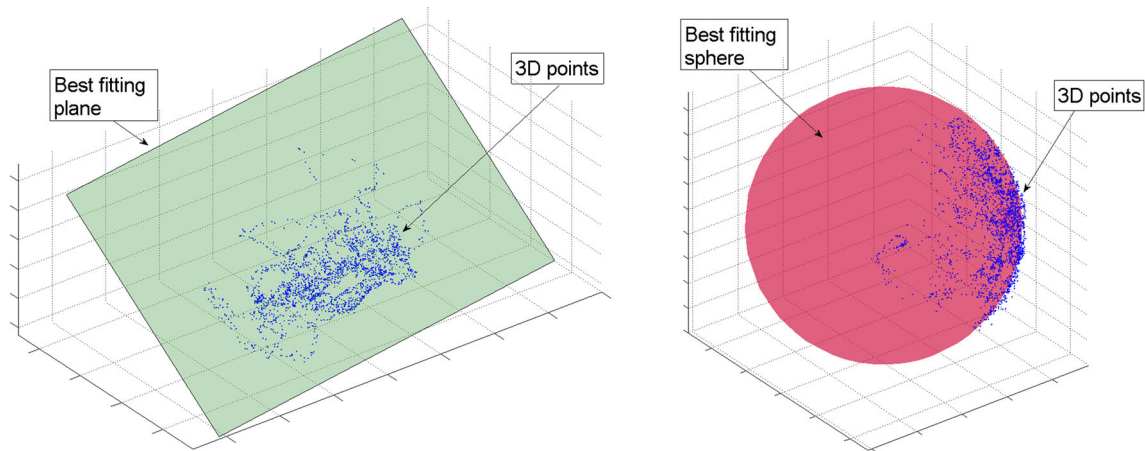


Fig. 10 Acquired 3D points and best fitting plane (*left*) and sphere (*right*)

Table 2 Summary of the registration accuracy for the three liver models

	Model 1	Model 2	Model 3
RMS error (mm)	1.30	1.73	1.41
Residual error (mm)	1.17 ± 0.56	1.47 ± 0.91	1.18 ± 0.76

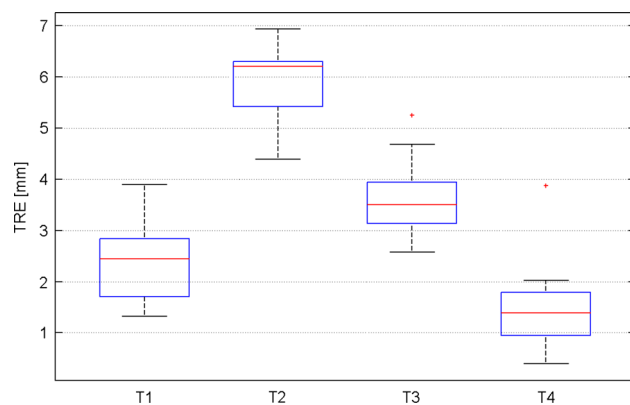


Fig. 11 Target registration errors for each target

age RMS matching error of 1.48 mm over all the points (Table 2). Additionally, by using four predefined landmarks on the surface of one liver phantom, the obtained TRE was 3.2 ± 0.57 mm. Figure 11 summarizes the registration error at the four target points, while Fig. 12 shows the displacement between the phantom (red) and the best (green) and worst (blue) registrations. Best and worst registrations were computed by defining the average of the four TREs for each registration attempt and by selecting, respectively, the minimum and the maximum values.

A sensitivity analysis was conducted, aiming at evaluating how different numbers of 3D points affect the registration accuracy. Figure 13 shows that the TRE decreased when using more 3D points. The lowest TRE (3.3 mm) was obtained by using 900 3D points. No significant differences

($\rho = 0.2$, using t test) were found between this TRE and the ones obtained with more than 600 points.

Discussion

This work presents a novel LRS-based IGS for laparoscopic liver procedures. A triangulation process is formulated that maps the LRS into IGS without knowing the laser depth information. This is particularly interesting since it allows the use of a compact and cost-effective LRS and therefore facilitates the integration into the clinical scenario. The LRS is composed of a commercial laser pointer, a trackable case, a standard laparoscope and an instrument tracking system. Patient-to-image registration is achieved by aligning the preoperative 3D model with the model reconstructed from the intraoperative laser scanning. Furthermore, the accuracy of the developed system, including the accuracy of automatic laser spot detection in the laparoscopic image, object reconstruction and registration of preoperative 3D volumes to liver phantoms, was demonstrated.

The LRS device was designed specifically with surgical integration aspects in mind: Limited additional instrumentation is required (a commercial laser pointer and sterilizable encasement as the only additional components) and automation of IGS-related activities (e.g., registration, instrument calibration). The LRS size and shape facilitate the handling and insertion into the laparoscopic incisions, while the preoperative LRS calibration and the automated registration procedure avoid additional intraoperative steps, thus simplifying the workflow. Experimental results show that the LRS can accurately detect the 2D coordinates of the laser in the laparoscopic image in 89% of cases in a variety of conditions. This aspect implies that the proposed method is robust even in the presence of reflections or induced artifacts. Further experiments show that the system is able to automatically

Fig. 12 Displacement of the best (*top*) and worst (*bottom*) registration on the *xy*, *xy*, *yz* planes

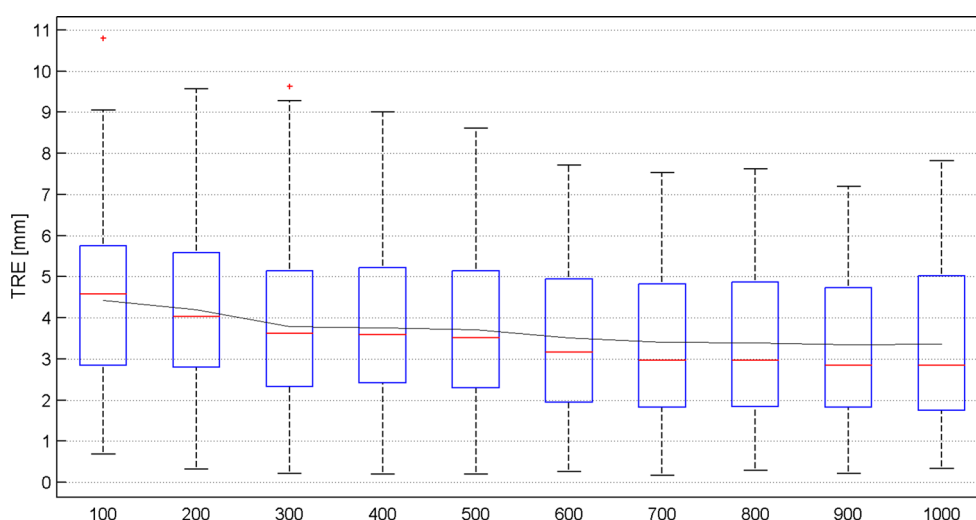
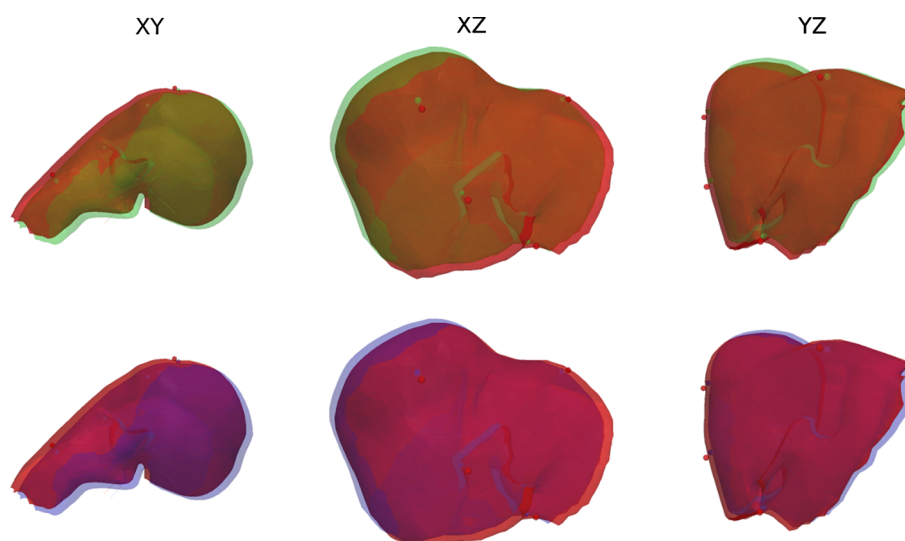


Fig. 13 Sensitivity analysis of the TRE by varying the number of 3D points. The *black line* represents the variation of the average TRE

register preoperative 3D volumes within an RMS error below 1.5 mm and an average TRE below 3.5 mm.

While the accuracy results presented within this work are similar to those previously reported, the proposed system is significantly smaller and more cost-effective (~100 USD including laser pointer, encasement) than the current commercially available LRS systems. More importantly, it is designed specifically for the use of laparoscopic liver procedures. These aspects should lead to a faster surgical integration than previous works. The intraoperative surface model is acquired by manually sweeping the laser over the liver; thus, the proposed system can be categorized as non-contact, manually swept registration method. The choice of opting for a manual sweep rather than automatic presents several advantages. Through a manual sweep, the surgeon can ensure that only the area of interest is scanned [6]. This diminishes the possibility of scanning surrounding organs

which would lead to an additional step aimed to remove these spurious 3D points from the dataset. Furthermore, a manual scanner provides higher flexibility compared to an automatic enlarging its clinical applicability to different areas. For example, by manually pointing at a specific target, the proposed system can aid in recovering the 3D position of critical structures, thus reducing problems related to loss of depth perception.

The registration procedure is expected to produce an accurate registration when the navigation system is positioned on the top of the OR table with the tracker over the patient's head. This constraint implies a constant surgical workflow, where the IGS is positioned at a similar location through different procedures. To account for the misplacement of the IGS and for the inpatient organ's shape variability, the coarse registration transforms the preoperative volume in the three most critical directions. Since the preoperative volume

is cropped, the rotation around the axis normal to the best fitting plane accounts for most of the inpatient shape variability. A rotation around the other two axes is computed in the fine registration because the edges of the cropped surface are easily found by the ICP and are sufficiently discriminant.

The accuracy in automatically detecting the laser spot in the laparoscope image cannot be compared with previous works, because no directly related quantitative information is reported. However, the implemented solution is robust over reflections or artifacts which often occur in a clinical scenario. The scanning precision of the presented LRS is inferior to the method presented in [15], while it is similar when compared with [6]. This discrepancy can be attributed to the distance from the LRS to the target (10–15 cm in the presented method, 2–6 cm in [15]). The accuracy of sphere reconstruction is similar to [13]. Additionally, a quantitative evaluation of the registration accuracy was presented, with an RMS accuracy and TRE sufficient for image-guided laparoscopic liver surgery. The TRE is smaller than the 10-mm safety margin suggested in [21]; therefore, the presented system might be useful during targeting procedures (e.g., ablation, biopsies). The robustness of the registration procedure is validated by the small displacement between the best and worst registration attempts as depicted in Fig. 12.

One potential drawback of the proposed LRS system is the time needed for scanning. It takes approximately one minute to scan 1000 3D points, which is higher than the previously reported solutions. This is due to the dependence of the presented LRS system to the laparoscope video stream, which limits the data acquisition rate to the laparoscope video frame rate. One possible solution to reduce the scanning time is to acquire fewer 3D points. As suggested in the sensitivity analysis conducted in the experiment, it is shown that our proposed methodology would guarantee a TRE below 4 mm by acquiring only 300 3D points instead of 600 thus reducing the scanning time to a few seconds, which is sufficient for clinical use. Another solution consists in the projection of a pattern rather than a single laser point which would increase the detection and acquisition of 3D points within each video frame.

Another shortcoming lies in the ICP-based rigid registration which is unable to recover for liver motion and deformation. While the assumption of a rigid transformation is valid in the presented phantom experiments, in a clinical scenario, additional future work will aim to compensate the liver deformation. Within laparoscopic liver procedures, liver deformation may appear due to respiratory motion, pneumoperitoneum pressure and instrument interaction with the liver. Based on the assumption that the largest respiratory-related liver movements occur in the cranio-caudal and anterior–posterior direction [22], a possible solution is the employment of a mechanical high-frequency jet ventilation (HFJV) system. By utilizing low tidal movements of

the lungs, HFJV has been shown to significantly reduce ventilation-related cranio-caudal movements of the liver from 20 to 5 mm [23,24]. Regarding deformation induced by the artificial pneumoperitoneum, initial studies showed an average liver displacement of 2.5 mm [25]. A more recent study showed a maximum liver displacement of 28 mm in the cranio-caudal direction; however, the displacement was found to be a rigid body transformation rather than a body deformation [26]. These studies suggest that liver deformation, due to pneumoperitoneum, is not as critical as in open liver procedures, where after liver exposure and surgical mobilization, non-rigid deformations may significantly change the intraoperative liver shape [27]. Nevertheless, liver deformation due to interaction with surgical instruments can be recovered with the employment of non-rigid registration methods. Within this context, the integration of statistical models for the characterization of liver motion and deformation [28] and the employment of non-rigid registrations would allow to compensate for this kind of deformation [29–32].

The presented work highlights the feasibility of a cost-effective and suitably sized LRS, and initial phantom experiments confirm sufficient accuracy for its use in clinical settings. However, to further validate this methodology, additional *in vitro* and *in vivo* validation experiments as presented in [33] will be performed in the future. In the future, the integration of LRS into a surgical scenario would allow fast registration of the liver with the preoperative image. Additionally, avoiding contact with the organ and thus preserving its initial shape would provide a higher similarity between the preoperative 3D volume and thus a more accurate registration. In case of liver shape changes during the surgery, a fast 3D point acquisition would also provide the possibility to compensate this tissue deformation intraoperatively. Finally, the application of LRS in laparoscopy would allow a real time measurement of the distance between the tracked instruments and vital organs, thus accounting for the loss of depth perception.

Conclusion

We have presented an alternative LRS for laparoscopic image guidance that is cost-effective and specifically designed for laparoscopic applications. The advantages of the proposed system are the specific design of an LRS for laparoscopic procedures enabled by a novel triangulation formulation, an automated workflow and a detailed evaluation of the methodology on liver phantoms. More specifically, the workflow is eased by the automatic registration method and by the pre-calibration of the instruments which decrease the workflow complexity and the steps required to perform the registration. The triangulation formulation allows for an easier recovery

of the 3D laser points and thus allows for a simpler instrumentation. The accuracy and the reliability of the registration method, which are evaluated on phantoms, are also compared with previous solutions.

The presented work represents a proof of concept of the employment of a compact and cost-effective LRS for registration in laparoscopic image guidance. Within this context, whereas the proposed system suffers from limitations such as the time required for scanning and the rigidity assumption of the registration method, different approaches are proposed to address these potential drawbacks.

In conclusion, we believe that this work highlights the usefulness and feasibility of this approach which represents a step toward the surgical integration of LRS for laparoscopic applications.

Acknowledgments The authors would like to acknowledge Denise Baumann, Tom Williamson, Dr. Kate Gavaghan for advice and CAScination AG for providing the IGS system used in the experiments.

Compliance with ethical standards

Conflict of interest Matteo Fusaglia, Hanspeter Hess, Marius Schwalbe, Matthias Peterhans, Pascale Tinguely, Stefan Weber and Huanxiang Lu declare that they have no conflict of interest.

Human and animal rights statement This article does not contain any studies with human participants performed by any of the authors.

References

- Sjølie E, Langø T, Ystgaard B, Tangen G, Nagelhus Hernes T, Mårvik R (2003) 3D ultrasound-based navigation for radiofrequency thermal ablation in the treatment of liver malignancies. *Surg Endosc* 17(6):933–938
- Hill DL, Batchelor P (2001) Registration methodology: concepts and algorithms, Biomedical engineering. In: Hajnal JV, Hill D, Hawkes D (eds) *Medical Image Registration*. CRC Press, London, pp 39–70
- Bao P, Warmath J, Galloway R Jr, Herline A (2005) Ultrasound-to-computer-tomography registration for image-guided laparoscopic liver surgery. *Surg Endosc Other Interv Tech* 19(3):424–429
- Herline AJ, Herring JL, Stefansic JD, Chapman WC, Galloway RL, Dawant BM (2000) Surface registration for use in interactive, image-guided liver surgery. *Comput Aided Surg* 5(1):11–17
- Lange T, Eulenstein S, Hünerbein M, Schlag P-M (2003) Vessel-based non-rigid registration of MR/CT and 3D ultrasound for navigation in liver surgery. *Comput Aided Surg* 8(5):228–240
- Lathrop RA, Hackworth DM, Webster RJ (2010) Minimally invasive holographic surface scanning for soft-tissue image registration. *Biomed Eng IEEE Trans* 57(6):1497–1506
- Audette MA, Siddiqi K, Ferrie FP, Peters TM (2003) An integrated range-sensing, segmentation and registration framework for the characterization of intra-surgical brain deformations in image-guided surgery. *Comput Vis Image Underst* 89(2):226–251
- Schlaier J, Warnat J, Brawanski A (2002) Registration accuracy and practicability of laser-directed surface matching. *Comput Aided Surg* 7(5):284–290
- McDonald CP, Brownhill JR, King GJ, Johnson JA, Peters TM (2007) A comparison of registration techniques for computer-and image-assisted elbow surgery. *Comput Aided Surg* 12(4):208–214
- Joskowicz L, Shamir R, Freiman M, Shoham M, Zehavi E, Umanovsky F, Shoshan Y (2006) Image-guided system with miniature robot for precise positioning and targeting in keyhole neurosurgery. *Comput Aided Surg* 11(4):181–193
- Cash DM, Sinha TK, Chapman WC, Terawaki H, Dawant BM, Galloway RL, Miga MI (2003) Incorporation of a laser range scanner into image-guided liver surgery: surface acquisition, registration, and tracking. *Med Phys* 30(7):1671–1682
- Dumpuri P, Clements LW, Dawant BM, Miga MI (2010) Model-updated image-guided liver surgery: preliminary results using surface characterization. *Prog Biophys Mol Biol* 103(2–3):197–207. doi:10.1016/j.pbiomolbio.2010.09.014
- Hayashibe M, Suzuki N, Nakamura Y (2006) Laser-scan endoscope system for intraoperative geometry acquisition and surgical robot safety management. *Med Image Anal* 10(4):509–519
- Hayashibe M, Suzuki N, Hattori A, Nakamura Y (2002) Intraoperative fast 3D shape recovery of abdominal organs in laparoscopy. In: *Medical image computing and computer-assisted intervention—MICCAI 2002*. Springer, pp 356–363
- Friets E, Bieszczad J, Kynor D, Norris J, Davis B, Allen L, Chambers R, Wolf J, Glisson C, Herrell SD, Galloway RL (2013) Endoscopic laser range scanner for minimally invasive, image guided kidney surgery. In: *SPIE medical imaging. International society for optics and photonics*, pp 867105–867108
- Hess-Flores M, Recker S, Joy K (2014) Uncertainty, baseline, and noise analysis for L1 error-based multi-view triangulation. In: *Pattern recognition (ICPR), 2014 22nd international conference on. IEEE*, pp 4074–4079
- Beraldin J-A (2004) Integration of laser scanning and close-range photogrammetry—the last decade and beyond. In: *Proceedings of the 20th congress international society for photogrammetry and remote sensing. Istanbul, Turkey*, pp 972–983
- Zhang Z (2000) A flexible new technique for camera calibration. *Pattern Anal Mach Intell IEEE Trans* 22(11):1330–1334
- Besl PJ, McKay ND (1992) Method for registration of 3-D shapes. In: *Proceedings of the SPIE 1611, sensor fusion IV: control paradigms and data structures, 586 (April 30, 1992)*. doi:10.1117/12.57955
- Arun KS, Huang TS, Blostein SD (1987) Least-squares fitting of two 3-D point sets. *Pattern Anal Mach Intell IEEE Trans* 5:698–700
- Mahnken AH, Ricke J (2009) CT-and MR-guided Interventions in Radiology, vol 22. Springer, New York
- Rohlfing T, Maurer CR Jr, O'Dell WG, Zhong J (2004) Modeling liver motion and deformation during the respiratory cycle using intensity-based nonrigid registration of gated MR images. *Med Phys* 31(3):427–432
- Biro P, Spahn D, Pfammatter T (2009) High-frequency jet ventilation for minimizing breathing-related liver motion during percutaneous radiofrequency ablation of multiple hepatic tumours. *Br J Anaesth* 102(5):650–653. doi:10.1093/bja/aep051
- Warner M, Warner M, Buck C, Segura J (1988) Clinical efficacy of high frequency jet ventilation during extracorporeal shock wave lithotripsy of renal and ureteral calculi: a comparison with conventional mechanical ventilation. *J Urol* 139(3):486–487
- Herline AJ, Stefansic JD, Debelak JP, Hartmann SL, Pinson CW, Galloway RL, Chapman WC (1999) Image-guided surgery: preliminary feasibility studies of frameless stereotactic liver surgery. *Arch Surg* 134(6):644–650. doi:10.1001/archsurg.134.6.644
- Zijlmans M, Langø T, Hofstad EF, Van Swol CF, Rethy A (2012) Navigated laparoscopy-liver shift and deformation due to pneumoperitoneum in an animal model. *Minim Invasive Ther Allied Technol* 21(3):241–248

27. Heizmann O, Zidowitz S, Bourquain H, Potthast S, Peitgen H-O, Oertli D, Kettelhack C (2010) Assessment of intraoperative liver deformation during hepatic resection: prospective clinical study. *World J Surg* 34(8):1887–1893
28. Blackall JM, King AP, Penney GP, Adam A, Hawkes DJ (2001) A statistical model of respiratory motion and deformation of the liver. In: *Medical image computing and computer-assisted intervention—MICCAI 2001*. Springer, pp 1338–1340
29. Schnabel JA, Rueckert D, Quist M, Blackall JM, Castellano-Smith AD, Hartkens T, Penney GP, Hall WA, Liu H, Truwit CL, Gerritsen FA, Hill DLG, Hawkes DJ (2001) A generic framework for non-rigid registration based on non-uniform multi-level free-form deformations. In: *Medical image computing and computer-assisted intervention—MICCAI 2001*. Springer, pp 573–581
30. Masutani Y, Kimura F (2001) Modally controlled free form deformation for non-rigid registration in image-guided liver surgery. In: *Medical image computing and computer-assisted intervention—MICCAI 2001*. Springer, pp 1275–1278
31. Li H, Sumner RW, Pauly M (2008) Global correspondence optimization for non-rigid registration of depth scans. *Comput Graph Forum* 27:1421–1430. doi:[10.1111/j.1467-8659.2008.01282.x](https://doi.org/10.1111/j.1467-8659.2008.01282.x)
32. Sinha TK, Dawant BM, Duay V, Cash DM, Weil RJ, Thompson RC, Weaver KD, Miga MI (2005) A method to track cortical surface deformations using a laser range scanner. *Med Imaging IEEE Trans* 24(6):767–781
33. Simpson AL, Burgner J, Glisson CL, Herrell SD, Ma B, Pfeiffer TS, Webster RJ, Miga M (2013) Comparison study of intraoperative surface acquisition methods for surgical navigation. *Biomed Eng IEEE Trans* 60(4):1090–1099